Dumbbell kinetic theory for polymers in a combination of flow and external electric field

Angelo C. Setaro and Patrick T. Underhill
The Howard P. Isermann Department of Chemical and Biological Engineering, Rensselaer Polytechnic Institute, Troy, New York 12180, USA

(Received 2 August 2019; published 4 November 2019)

Combining Poiseuille flow with an external electric field is a demonstrated method to drive transverse migration in capillary electrophoresis. Despite both computational and experimental studies, a number of questions about how to best model polymers under these conditions remains. Attempts have been made to develop a kinetic theory for a bead-spring dumbbell model, but these have only been accurate at low electric field strength and have not captured the nonmonotonic relationship between migration and electric field strength. In this paper, we revisit the development of a kinetic theory for a bead-spring dumbbell in a combination of parabolic flow and an external electric field. The resultant theory yields a compact formula that predicts polymer concentration profiles that agree excellently with our Brownian dynamics simulations including the aforementioned nonmonotonic relationship. Furthermore, we compare our theoretical results to experimental data and find that our model nearly quantitatively predicts the position of the maximum in migration.

DOI: 10.1103/PhysRevE.100.052501

I. INTRODUCTION

It has been found that in parallel or antiparallel external pressure-driven flow and electric field, DNA migrates perpendicular to the flow and field [1,2]. Understanding the mechanism for this phenomena could guide the development of the next generation of microfluidic devices and allow for the manipulation and study of individual molecules with a high degree of control. When flexible polymers are exposed to pressure-driven flow in a channel (without an electric field), the polymers will migrate towards the center [3,4]. This migration is understood to be hydrodynamically driven in nature [5,6]. However, this mechanism is not strong enough to explain the migration of DNA in the experiments with electric fields.

It is believed that the migration of DNA in both flow and field is due to electrohydrodynamic interactions (EHIs) between parts of the DNA [7]. These interactions lead to a electrophoretic mobility tensor that depends on conformation. The use of combined flow and electric fields has been to successfully trap and separate molecules by manipulating their conformation dependent mobility [8–10] as well as concentrate genomic length DNA [11].

To date, there have been two major approaches to incorporate EHI into the modeling flexible polyelectrolytes. One, developed by Liao *et al.* [12], discarded the long-range electrohydrodynamic interactions, opting instead to include only those interactions on a scale of a Kuhn length. The one-dimensional model was successfully used to understand qualitative changes in conformation dependent mobility as a function of electric field strength. However, this model assumed that the polymer was strongly stretched in the field direction and could not capture transverse migration. This model was later generalized by Pandey and Underhill [13] and later used to understand the trapping of flexible polyelectrolytes in T channels [8]. These coarse-grained models take the form of a bead-spring chain in which the mobility of a spring depends on the conformation of the spring. In this way, they incorporate the EHI between polymer segments within a spring.

The other approach, developed by Kekre and co-workers is a bead-spring chain model that directly includes long-range EHI between segments [14]. This method captures the fluctuations of the electrophoretic mobility as the conformation fluctuates and includes the long-range interactions that are important near equilibrium when the polymer is only weakly deformed. However, representing polymers that are stretched far from equilibrium would require a large number of springs, all interacting with one another. This would greatly increase the computational cost of using such a model.

Montes *et al.* [10] and Arca *et al.* [11] have successfully used their model to quantify the dynamics and migration in devices with combinations of fluid flow and electric field. This includes currently capturing the nonmonotonic dependence of the amount of migration on the strength of the electric field. They also developed a kinetic theory for a bead-spring dumbbell model in a combination of parabolic flow and an external force [15]. Although their kinetic theory accurately predicts migration at low electric field strengths, it incorrectly predicts a monotonic relationship between electric field strength and migration. This has led to questions regarding the mechanism for the nonmonotonic trend and why the bead-spring chain with direct interactions captures it, but the kinetic theory of a coarse-grained dumbbell does not.

In this article, we show using Brownian dynamics (BD) simulations that a bead-spring dumbbell model is sufficient to capture the nonmonotonic relationship between electric field strength and migration for a variety of flow strengths. Furthermore, we show that a modified derivation of the kinetic

theory captures this nonmonotonic relationship in agreement with our BD simulations.

II. SIMULATION METHOD

A standard BD method [16–18] was utilized for this research. The polymer was reduced to a bead-spring dumbbell, whereas the solvent was represented by a continuum, which accounted for the stochastic motion and the viscous drag. Note that explicit hydrodynamic interactions have not been included. The positions of the beads are denoted by $\mathbf{r}_1$ and $\mathbf{r}_2$. During each time step, a series of forces are applied to each bead to determine their motion. The polymers are exposed to a fully developed Poiseuille flow in x and varying in y. Furthermore, the system includes a uniform electric field pointing in the x direction. The dynamical equations take the form

$$d\boldsymbol{r}_1 = \left[\boldsymbol{u}^f(\boldsymbol{r}_1) + \boldsymbol{\mu}\cdot\boldsymbol{E} + \frac{1}{\zeta}\boldsymbol{F}_s\right]dt + \sqrt{\frac{2k_BT\,dt}{\zeta}}d\boldsymbol{W}_1, \quad (1)$$

$$d\boldsymbol{r}_2 = \left[\boldsymbol{u}^f(\boldsymbol{r}_2) + \boldsymbol{\mu}\cdot\boldsymbol{E} - \frac{1}{\zeta}\boldsymbol{F}_s\right]dt + \sqrt{\frac{2k_BT\,dt}{\zeta}}d\boldsymbol{W}_2, \quad (2)$$

where $\boldsymbol{u}^f$ is the external fluid flow, $\boldsymbol{\mu}$ is the electrophoretic mobility tensor, $\boldsymbol{E}$ is the external electric field, ζ is the bead drag coefficient, $\boldsymbol{F}_s$ is the spring force, k_B is the Boltzmann constant, T is the absolute temperature, dt is the time step, and $d\boldsymbol{W}_1$ and $d\boldsymbol{W}_2$ are vectors with components that are independent stochastic variables chosen from a distribution with zero mean and a variance of 1. We define the spring connecter vector as $\boldsymbol{Q} = \boldsymbol{r}_2 - \boldsymbol{r}_1$ and the center-of-mass as $\boldsymbol{r}_c = (\boldsymbol{r}_2 + \boldsymbol{r}_1)/2$.

The springs make use of the finitely extensible nonlinear elastic (FENE) spring force law [19], which is given by

$$\boldsymbol{F}_s = \frac{H_{\rm spr}\boldsymbol{Q}}{1-f^2}, \quad (3)$$

where $f = |\boldsymbol{Q}|/Q_0$ is the spring's fractional extension, Q_0 is the maximal extension of the spring, and $H_{\rm spr}$ is the spring constant.

The coarse-grained mobility tensor for a FENE spring is given by [13]

$$\boldsymbol{\mu} = \left(\mu_0 + \frac{4\mu_1 f^2}{3-f^2}\right)\hat{\boldsymbol{Q}}\hat{\boldsymbol{Q}} + \left(\mu_0 - \frac{2\mu_1 f^2}{3-f^2}\right)(\boldsymbol{I} - \hat{\boldsymbol{Q}}\hat{\boldsymbol{Q}}), \quad (4)$$

where $\boldsymbol{I}$ is the identity tensor, $\hat{\boldsymbol{Q}} = \boldsymbol{Q}/Q$, μ_0 is the mobility of the polymer at equilibrium, and μ_1 is related to the mobility of the polymer away from equilibrium due to EHI between polymer segments.

For all the cases examined here, the fractional extension of the springs is small enough that the results are the same as with a Hookean spring with the force law,

$$\boldsymbol{F}_s \approx H_{\rm spr}\boldsymbol{Q}, \quad (5)$$

with an approximate Hookean mobility tensor given by

$$\boldsymbol{\mu} \approx \left(\mu_0 - \frac{2}{3}\mu_1 f^2\right)\boldsymbol{I} + 2\mu_1 f^2\hat{\boldsymbol{Q}}\hat{\boldsymbol{Q}}. \quad (6)$$

For this paper, the external fluid flow is parabolic, so the flow profile is given by

$$u_x^f = \bar{\gamma}H[1-(y/H)^2], \quad (7)$$

where $\bar{\gamma}$ is the average shear rate, y is the distance from the channel center, and H is the channel's half height with the walls at $y = H$ and $y = -H$. We quantify the strength of the fluid flow using a flow Weissenberg number, defined as $\mathrm{Wi}_F = \bar{\gamma}\tau$, where τ is the Rouse relaxation time given by $\tau = \zeta/4H_{\rm spr}$. Due to the fact that the electric field is uniform, we cannot use a field gradient to define an electric Weissenberg number. Rather, we define Wi_E such that $\mathrm{Wi}_E = \mathrm{Wi}_F$ corresponds to the case that $\mu_0 E$ equals the mean fluid flow. Using the relationship between the average shear rate and the mean fluid flow, this results in $\mathrm{Wi}_E = 3\mu_0 E\tau/(2H)$.

III. KINETIC THEORY

The kinetic theory for an uncharged dumbbell in a channel in dilute solution was developed in Ref. [4]. Later, this theory was generalized to include an external force in Ref. [15]. For the sake of brevity, only the essential points are elucidated here.

The steady-state distribution for a polymer dumbbell in solution is given by the distribution function $\boldsymbol{\Psi}$, which is a function of the center-of-mass $\boldsymbol{r}_c$ and the end-to-end vector $\boldsymbol{Q}$, and satisfies the conservation equation,

$$0 = -\frac{\partial}{\partial \boldsymbol{r}_c}\cdot(\dot{\boldsymbol{r}}_c\boldsymbol{\Psi}) - \frac{\partial}{\partial \boldsymbol{Q}}\cdot(\dot{\boldsymbol{Q}}\boldsymbol{\Psi}), \quad (8)$$

where $\dot{\boldsymbol{r}}_c$ and $\dot{\boldsymbol{Q}}$ can be determined by combining Eqs. (1) and (2),

$$\dot{\boldsymbol{r}}_c = \frac{\boldsymbol{u}^f(\boldsymbol{r}_1) + \boldsymbol{u}^f(\boldsymbol{r}_2)}{2} + \boldsymbol{\mu}\cdot E - \frac{D_b}{2}\frac{\partial \ln \boldsymbol{\Psi}}{\partial \boldsymbol{r}_c}, \quad (9)$$

$$\dot{\boldsymbol{Q}} = \boldsymbol{u}^f(\boldsymbol{r}_2) - \boldsymbol{u}^f(\boldsymbol{r}_1) - \frac{2}{\zeta}\boldsymbol{F}_s - 2D_b\frac{\partial \ln \boldsymbol{\Psi}}{\partial \boldsymbol{Q}}, \quad (10)$$

where $D_b = k_BT/\zeta$ is the bead diffusivity. It is worth noting that previous studies assumed that two terms in Eq. (8) are both independently near zero due to the polymer's rapid connector vector equilibration relative to migration [15]. We do not make that assumption here.

The probability distribution is then decomposed into a center-of-mass distribution function n and end-to-end distribution function ψ,

$$\boldsymbol{\Psi}(\boldsymbol{r}_c, \boldsymbol{Q}) = n(\boldsymbol{r}_c)\psi(\boldsymbol{r}_c, \boldsymbol{Q}), \quad (11)$$

where

$$n(\boldsymbol{r}_c) = \int \boldsymbol{\Psi}(\boldsymbol{r}_c, \boldsymbol{Q})d\boldsymbol{Q}. \quad (12)$$

If Eq. (8) is integrated over $\boldsymbol{Q}$, the steady-state distribution of the center of mass can be written

$$\frac{\partial}{\partial \boldsymbol{r}_c}\cdot(n\langle\dot{\boldsymbol{r}}_c\rangle) = 0, \quad (13)$$

where the angle brackets $\langle\,\rangle$ represent an average over $\boldsymbol{Q}$ using the conditional distribution ψ.

Plugging Eq. (9) into Eq. (13) and using a Taylor expansion of the flow yields

$$0 = \frac{\partial}{\partial \boldsymbol{r}_c} \cdot \left[n\boldsymbol{u}^f(\boldsymbol{r}_c) + \frac{n}{8}\langle \boldsymbol{QQ}\rangle : \left(\frac{\partial}{\partial \boldsymbol{r}} \frac{\partial}{\partial \boldsymbol{r}} \boldsymbol{u}^f \right)\Big|_{\boldsymbol{r}=\boldsymbol{r}_c} + n\langle \boldsymbol{\mu}\rangle \cdot \boldsymbol{E} - \frac{D_b}{2}\frac{\partial n}{\partial \boldsymbol{r}_c}\right]. \tag{14}$$

Due to the form of the flow field and electric field used here, Eq. (14) simplifies to

$$\frac{d}{dy}\left[n\langle \mu_{yx}\rangle E - \frac{D_b}{2}\frac{dn}{dy}\right] = 0, \tag{15}$$

where $\langle \mu_{yx}\rangle$ is the averaged yx component of the mobility tensor and y is the component of the center-of-mass position. Because n only depends on y, it has been renormalized to a one-dimensional probability distribution. Inside the brackets is the net y component of the translational flux of dumbbells. It can be seen that the flux is determined by the sum of the EHI migration and the counteracting diffusion term. The boundary conditions require that the flux at the walls is zero, leading to

$$\frac{d\ \ln(n)}{dy} = \frac{2}{D_b}\langle \mu_{yx}\rangle E. \tag{16}$$

To simplify our analysis, we use a Hookean spring and approximate mobility for the kinetic theory. The yx component for the Hookean mobility [Eq. (6)] is given by

$$\langle \mu_{yx}\rangle = \frac{2\mu_1}{Q_0^2}\langle Q_x Q_y\rangle. \tag{17}$$

Plugging this into Eq. (16) yields

$$\frac{d\ \ln(n)}{dy} = \frac{4\mu_1 E}{D_b Q_0^2}\langle Q_x Q_y\rangle. \tag{18}$$

The concentration profile is, therefore, related to the second order xy moment of the spring connector vector. In order to determine the second order moments, Eq. (8) is multiplied by $\boldsymbol{QQ}$ and integrated over $\boldsymbol{Q}$. The term with the $\boldsymbol{Q}$ derivative can be manipulated using standard integration by parts manipulations from Ref. [20]. The shear, spring, and Brownian diffusion contributions in Eq. (10) lead to corresponding terms in the moment equation.

The center-of-mass terms can be simplified using

$$n\langle \dot{\boldsymbol{r}}_c \boldsymbol{QQ}\rangle = n\boldsymbol{u}^f\langle \boldsymbol{QQ}\rangle + \frac{n}{8}\left\langle \boldsymbol{QQ} : \left(\frac{\partial}{\partial \boldsymbol{r}} \frac{\partial}{\partial \boldsymbol{r}} \boldsymbol{u}^f \right)\Big|_{\boldsymbol{r}=\boldsymbol{r}_c} \boldsymbol{QQ}\right\rangle + n\langle \boldsymbol{\mu}\cdot\boldsymbol{E}\boldsymbol{QQ}\rangle - \frac{D_b}{2}\frac{\partial}{\partial \boldsymbol{r}_c} n\langle \boldsymbol{QQ}\rangle. \tag{19}$$

In order to nondimensionalize our system, we scale channel quantities by $(3k_BT/H_{\rm spr})^{1/2}$ while scaling the spring vector by $(k_BT/H_{\rm spr})^{1/2}$. Therefore, we define $\tilde{y} = y/(3k_BT/H_{\rm spr})^{1/2}$, $\tilde{H} = H/(3k_BT/H_{\rm spr})^{1/2}$, and $\tilde{\boldsymbol{Q}} = \boldsymbol{Q}/(k_BT/H_{\rm spr})^{1/2}$. Applying these definitions to Eq. (18) results in

$$\frac{d\ \ln(\tilde{n})}{d\tilde{y}} = \Phi\langle \tilde{Q}_x\tilde{Q}_y\rangle, \tag{20}$$

where $\tilde{n} = n(3k_BT/H_{\rm spr})^{1/2}$ and

$$\Phi = 32\tilde{H}\mu_1 {\rm Wi}_E/(\mu_0 b) = \frac{16\tau\mu_1 E}{Q_0^2}\sqrt{\frac{3k_BT}{H_{\rm spr}}}. \tag{21}$$

The FENE parameter $b = H_{\rm spr}Q_0^2/(k_BT)$ is three times the number of Kuhn segments in the chain. The parameter Φ is a key dimensionless group that is proportional to the electric field and determines the migration. It quantifies the balance between the two fluxes present in Eq. (15) by which the deviation of the spring distribution from equilibrium creates an electrophoretic flux that is balanced by a diffusive flux to determine the overall concentration profile. Equation (20) quantifies the relationship between the concentration profile and the conformation distribution. Further insight into the mechanism of migration is gleaned by developing expressions for the second order moments, which can also be nondimensionalized. The necessary yx, xx, and yy components are

$$24\tilde{n}\left[\langle \tilde{Q}_y^2\rangle\tilde{\gamma} - \langle \tilde{Q}_x\tilde{Q}_y\rangle\right] = \Phi\frac{d}{d\tilde{y}}\left(\tilde{n}\langle \tilde{Q}_x^2\tilde{Q}_y^2\rangle\right) - \frac{d^2}{d\tilde{y}^2}\left(\tilde{n}\langle \tilde{Q}_x\tilde{Q}_y\rangle\right), \tag{22}$$

$$24\tilde{n}[1 - \langle \tilde{Q}_y^2\rangle] = \Phi\frac{d}{d\tilde{y}}\left(\tilde{n}\langle \tilde{Q}_x^3\tilde{Q}_y\rangle\right) - \frac{d^2}{d\tilde{y}^2}\left(\tilde{n}\langle \tilde{Q}_y^2\rangle\right), \tag{23}$$

and

$$24\tilde{n}\left[2\langle \tilde{Q}_x\tilde{Q}_y\rangle\tilde{\gamma} - \langle \tilde{Q}_x^2\rangle + 1\right] = \Phi\frac{d}{d\tilde{y}}\left(\tilde{n}\langle \tilde{Q}_x\tilde{Q}_y^3\rangle\right) - \frac{d^2}{d\tilde{y}^2}\left(\tilde{n}\langle \tilde{Q}_x^2\rangle\right), \tag{24}$$

where

$$\tilde{\gamma} = \dot{\gamma}\tau = 2\frac{\bar{\gamma}\tilde{y}}{\tilde{H}}\tau = \frac{2\,{\rm Wi}_F\tilde{y}}{\tilde{H}}. \tag{25}$$

These equations yield insight into the phenomena that impact the second order moments. In particular, Eq. (22) describes the mechanisms that determine $\langle \tilde{Q}_x\tilde{Q}_y\rangle$, which then determines the concentration profile via Eq. (20). The value of $\langle \tilde{Q}_x\tilde{Q}_y\rangle$ is determined by a balance of shear, represented by the $\langle \tilde{Q}_y^2\rangle\tilde{\gamma}$ term, an electric field migratory flux, represented by the Φ term, and a diffusive flux, represented by the second derivative term. The importance of these terms varies as a function of electric field strength as will be discussed in the following section and shown schematically in Fig. 1.

As mentioned earlier, previous kinetic theories examining migration of polymer dumbbells simplified the system by assuming that the polymer's connector vector distribution relaxed quickly compared to the polymer's migration across the channel. If that approximation is performed, the right hand sides of Eqs. (22)–(24) are zero.

IV. RESULTS AND DISCUSSION

A. Brownian dynamics simulations

For the simulations presented here, we used dumbbell bead springs. The channel width was chosen to correspond to a physical channel with a width of 80 μm containing λ DNA. This corresponds to $\tilde{H} = 21.775$. The length of the chain was such that $b = 450$, which is roughly equivalent to the length of labeled λ DNA [21]. Each simulation had three polymers with

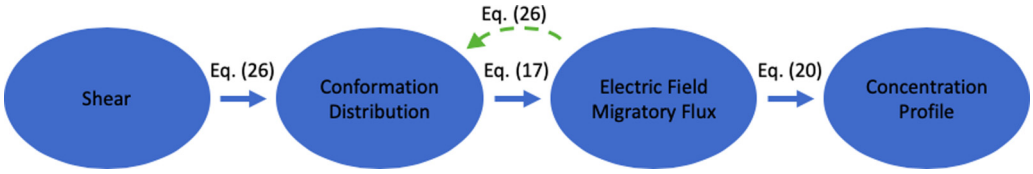

FIG. 1. A schematic for the mechanism of migration. The solid arrows illustrate how the phenomena affect each other. The arrow labels refer to the corresponding equations where the relationship is demonstrated. The dashed green arrow highlights the new phenomenon incorporated in our kinetic theory that is important at intermediate and high electric field strengths.

a μ_1/μ_0 of 0.125 were simulated and was run using a forward Euler integration scheme for 10^6 steps where $dt = 10^{-3}\tau$.

By tracking the center of mass of each spring over the course of the simulation, we are able to generate the probability distribution for the polymers across the channel. A series of example distributions are shown in Fig. 2 for a variety of Wi_F's and Wi_E's, which we fit with a normalized Gaussian profile. The standard deviation was determined from this fitting and used to quantify the amount of migration. From the figure, we can see that the migration increases as Wi_E increases from 1 to 25 as evidenced from the tighter distributions. For Wi_E's greater than 25, the distributions begin to widen again, signifying a decrease in the amount of migration. The presence of a maximum of migration is consistent with experiment. The dimensionless standard deviation $\tilde{\sigma} = \sigma/(3k_BT/H_{\mathrm{spr}})^{1/2}$ from these profiles are shown in Fig. 3 in blue. We also simulated a number of other larger Wi_F's also shown in Fig. 3. The results show that the shape of the migration curves as well as the position of the minimum in $\tilde{\sigma}$ is unaffected by changes in Wi_F. However, the overall amount of migration at a given Wi_E is strongly impacted by the Wi_F with larger Wi_F's corresponding to larger amounts of migration. The curves in Fig. 3 are the results of the kinetic theory prediction developed in the following section.

To summarize, the BD simulations show that using a dumbbell model produces a nonmonotonic relationship between migration and electric field strength, which is consistent with experiment [9]. Because previous approximate kinetic theories based on a dumbbell model showed a monotonic trend, it was thought that a dumbbell model was insufficient to match with experiments [9,15]. Our results suggest that the discrepancy may have been due to the approximation in the kinetic theory instead of the use of a dumbbell model.

B. Solving the kinetic theory

The kinetic theory, Eqs. (22)–(24), did not make additional assumptions beyond Eq. (8) but do require knowledge of the

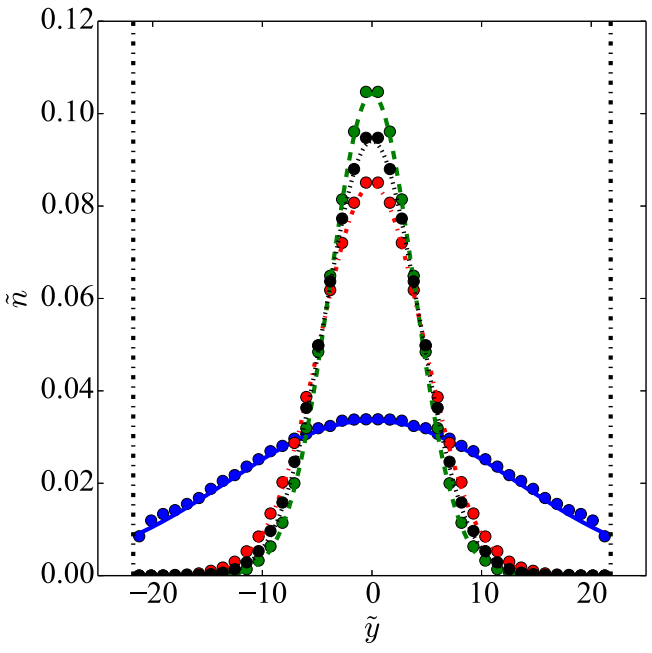

FIG. 2. The distribution of polymers across a series of simulations with different Wi_E's. The circles represent the amount of polymer in that region of the channel from the BD simulations. The curves are a Gaussian fit to the profiles. All simulations were run using $\mathrm{Wi}_F = 0.3$. The values of Wi_E are $\mathrm{Wi}_E = 1$ (blue line), $\mathrm{Wi}_E = 10$ (red dot-dashed line), $\mathrm{Wi}_E = 25$ (green dashed line), $\mathrm{Wi}_E = 50$ (black dotted line). The walls of the channel are represented by the vertical dot-dashed lines.

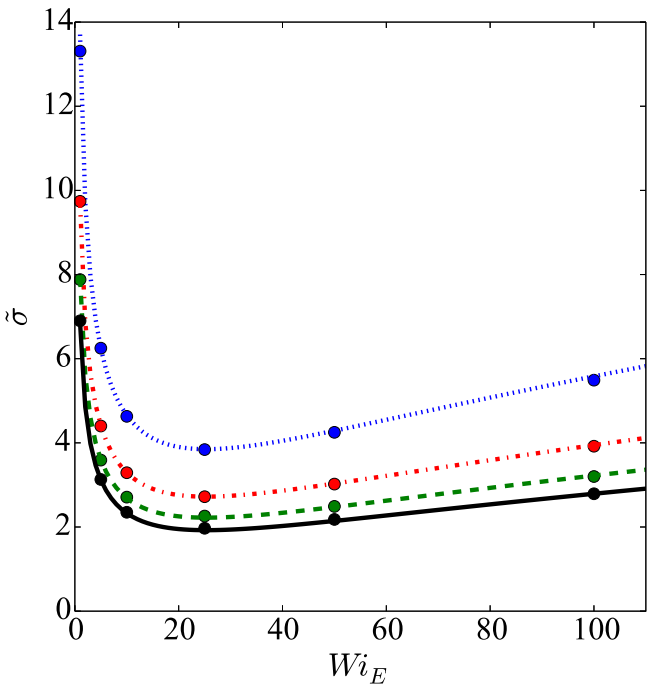

FIG. 3. Standard deviation of polymer concentration profiles. The solid circles are the calculated $\tilde{\sigma}$'s from our BD simulations: $\mathrm{Wi}_F = 0.3$ (blue dotted line), $\mathrm{Wi}_F = 0.6$ (red dot-dashed line), $\mathrm{Wi}_F = 0.9$ (green dashed line), and $\mathrm{Wi}_F = 1.2$ (black line). The lines are Eq. (27) for the corresponding value of Wi_F: $\mathrm{Wi}_F = 0.3$, $\mathrm{Wi}_F = 0.6$, $\mathrm{Wi}_F = 0.9$, and $\mathrm{Wi}_F = 1.2$.

fourth order moments to solve. Unfortunately, deriving the fourth order moments in the same manner used for the second order moments results in a larger system of equations that depend, in turn, on the sixth order moments. Appendix A describes a different type of closure approximation valid in weak flows which allows the equations to be solved. For most of the results shown here, a simpler approach is accurate in which the fourth order moments take their equilibrium values, which, in our nondimensionalization, are $\langle \tilde{Q}_x^2 \tilde{Q}_y^2 \rangle \approx 1$ and $\langle \tilde{Q}_x^3 \tilde{Q}_y \rangle \approx \langle \tilde{Q}_x \tilde{Q}_y^3 \rangle \approx 0$. Appendix B uses the BD simulations to show that the diffusive flux terms (second derivative terms) in Eqs. (22)–(24) are small for the cases examined here. Once the simplifications are applied, Eq. (23) becomes $\langle \tilde{Q}_y^2 \rangle = 1$ and Eq. (22) now takes the form

$$24\tilde{n}[\tilde{\gamma} - \langle \tilde{Q}_x \tilde{Q}_y \rangle] = \Phi \frac{d}{d\tilde{y}} \tilde{n}, \tag{26}$$

which is coupled with Eq. (20). The loss of the second derivative leads to boundary layers at the walls, but they do not affect the migration in the channel center when the width of the distribution is small compared to the channel width.

Figure 1 shows a schematic that illustrates the mechanism of migration. Equation (26) incorporates how the conformational distribution is determined by a combination of the shear (via $\tilde{\gamma}$) and the electrophoretic flux (via Φ). The conformation, in turn, determines the electrophoretic mobility via Eq. (17) which manifests as electrophoretic fluxes in Eqs. (20) and (26). Because the electric field migratory flux impacts the conformation distribution [green arrow in Fig. 1], it acts as a feedback mechanism. The impact of this feedback is more clearly seen if the derivative on the right hand side of Eq. (26) is eliminated using Eq. (20), and the resulting equation is solved to obtain

$$\langle \tilde{Q}_x \tilde{Q}_y \rangle = -\frac{48\,\mathrm{Wi}_F \tilde{y}}{\tilde{H}(24 + \Phi^2)}. \tag{27}$$

This result can then be plugged into Eq. (20) in order to determine the concentration profile and by extension the $\tilde{\sigma}$. Because the shear rate is linear, the function $\ln(n)$ becomes quadratic corresponding to a Gaussian profile with

$$\tilde{\sigma} = \left(\frac{\tilde{H}(24 + \Phi^2)}{48\,\mathrm{Wi}_F \Phi} \right)^{1/2}. \tag{28}$$

Equation (28) is plotted for a range of Wi_F in Fig. 3 in comparison with the BD simulations. There is excellent agreement between our simulated data and Eq. (28). Unlike previous kinetic theory models, our model is accurate at both low and high electric field strengths and accurately predicts the nonmonotonic relationship between the migration and the electric field strength. That being said, the error increases with increasing Wi_F. This is not surprising as the stronger flows are better able to push polymers out of equilibrium, which reduces the validity of the assumption that the fourth moments are near their equilibrium values.

From our formula for $\tilde{\sigma}$, we can determine the point of maximal migration for a given Wi_E and Wi_F. From Eq. (28), we find that $\Phi_{\min} = \sqrt{24}$ and

$$\min(\mathrm{Wi}_E) = \frac{\sqrt{24}}{32} \frac{\mu_0 b}{\mu_1 \tilde{H}}, \tag{29}$$

from which we see that the position of the minimum is independent of Wi_F as seen in Fig. 3. Furthermore, we can use Eqs. (28) and (26) to understand the physical mechanism for the nonmonotonic trend. For $\Phi \ll \sqrt{24}$, the migration contribution in Eq. (26) is small, and the second spring moment is determined by the shear flow. However, for $\Phi \gg \sqrt{24}$, the second spring moment decays as Φ^{-2}. Simultaneously, $d\tilde{n}/d\tilde{y}$ scales as Φ^{-1} such that the migration contribution in Eq. (26) balances the shear flow. In this way, the migration is self-limiting as the balance among the terms in Eq. (26) shifts depending on the strength of the electric field.

C. Relation to experiment

Section IV B showed that there was excellent agreement between our theory and BD simulations. However, it does not give insight to how well the mechanism in the theory explains the nonmonotonic trend seen in the experimental data. To determine this, we extracted the experimental migration data, consisting of the electric field strength and $\tilde{\sigma}$'s from Ref. [9]. More specifically, we used the data from Fig. 8 of Ref. [9] for the S1 [40 mM Tris-acetate-EDTA (TAE)] and S2 (0.4 mM TAE and 0.1 mM NaCl) solutions at $\mathrm{Wi}_F = 0.6$. These two solution conditions were chosen due to their different ionic strengths and Debye lengths. From the data, the corresponding electric field strengths were calculated. We used the electric field strength in conjunction with the channel size ($\tilde{H} = 21.775$), molecule size ($b = 450$), and molecule relaxation time ($\tau = 0.1$ s) to calculate Wi_E in accordance with the definition given earlier in this paper, instead of the definition given in Ref. [9]. The dimensionless results are plotted in Fig. 4(a) for the S1 data and in Fig. 4(b) for the S2 data.

To determine how well our model could reproduce the nonmonotonic trend, a least squared fitting was performed on both data sets using Eq. (27) with μ_1/μ_0 as the fitting parameter and $\mathrm{Wi}_F = 0.5$. The best fit plots are shown in Fig. 4 in green solid curves. The best fit values are $\mu_1/\mu_0 = 1.24$ for the S1 solution and $\mu_1/\mu_0 = 5.13$ for the S2 solution. These values represent how the conformation dependent mobility due to EHI appears in the coarse-grained model and varies with ionic strength. It is also worth noting that the experiments take place in a channel with a square cross section, whereas the theory examined a cross section with one dimension much larger than the other. Within these differences and the use of a coarse-grained model, the kinetic theory matches the migration and turnaround nearly quantitatively. In Refs. [12,13], the ratio μ_1/μ_0 is interpreted in terms of the mobility of a Kuhn segment parallel and perpendicular to the rod. In that interpretation, μ_1/μ_0 is expected to be less than or equal to 1/4 and applies to situations with large enough fractional extension so that long-ranged EHI is negligible. In this article, using Eqs. (4) and (6), the fractional extension is relatively small so that the ratio μ_1/μ_0 also incorporates contributions from long-ranged EHI in a coarse-grained way.

Recall that the nonmonotonic trend is due to the inclusion of an additional term in the kinetic theory. To illustrate the importance of that term in matching with the experimental data, we will also show the corresponding prediction if that

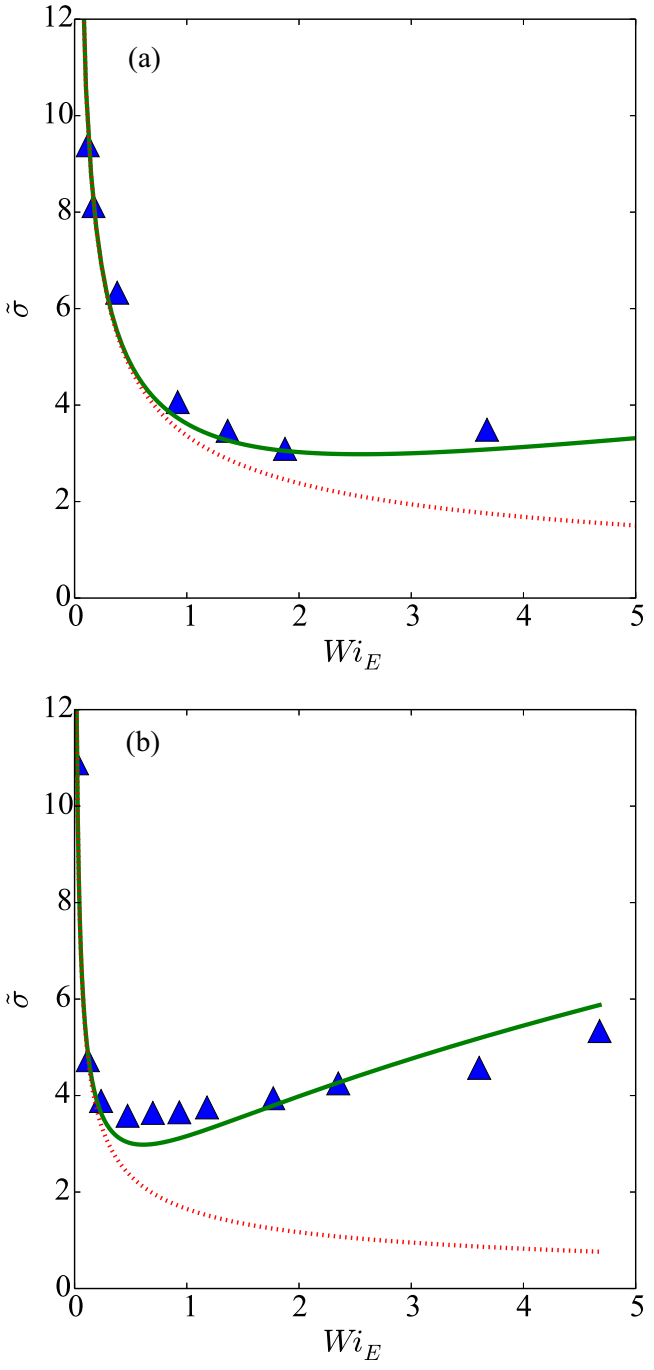

FIG. 4. Comparison of experimental data from Ref. [9]. The blue triangles are the experimental data with the S1 solution at $\mathrm{Wi}_F = 0.6$ shown in (a) and S2 solution at $\mathrm{Wi}_F = 0.6$ shown in (b). The best fit plots of Eq. (28) (green line) give a μ_1/μ_0 of 1.24 for the S1 solution and 5.13 for the S2 solution. Equation (30) is plotted using the corresponding best fit value for μ_1/μ_0 (red dotted line).

mechanism was not included. Previous investigators assumed that the polymer's connector vector distribution relaxed quickly compared to polymer migration across the channel. This assumption results in the right hand side of Eqs. (22)–(24) becoming zero. This different set of equations results in a prediction similar to Eq. (28) of the form

$$\tilde{\sigma} = \left(\frac{\tilde{H}}{2\,\mathrm{Wi}_F\,\Phi} \right)^{1/2}. \tag{30}$$

Equation (30) was then plotted using the same parameters and the best fit value of μ_1/μ_0. This is shown by the red dotted curves in Fig. 4. As can be seen from the figures, there is excellent agreement between Eqs. (28) and (30) at low Wi_E. However, as Wi_E (and by extension Φ) increases, the two equations deviate with Eq. (28) capturing the minimum near the experimental values, whereas Eq. (30) continues to decrease monotonically.

V. CONCLUSIONS

In this paper, we have quantified the migration due to the conformation dependent mobility of a coarse-grained dumbbell model in a combination of parabolic flow and an external electric field. We have shown that BD simulations making use of a coarse-grained dumbbell are capable of capturing the nonmonotonic relationship between migration and Wi_E. This result is in contrast to the predictions made from a previous kinetic theory. To gain mechanistic insight into the migration, we then developed a kinetic theory for the dumbbell bead spring. Via assumptions about the nature of the moments and the magnitude of the individual components, we were able to develop a compact formula for the amount of migration. This approximation [Eq. (28)] agreed excellently with our simulations across all of the Wi_F's and Wi_E's examined here.

Furthermore, the form of the differential equation in Eq. (26) yields insight into the underlying phenomenon determining the amount of migration. More specifically, the migration is determined by the balance of the shear flow trying to distort the spring distribution from equilibrium, the spring force resisting that distortion, and the electrophoretic mobility migrating the polymers across regions with different shear rates. When varying the electric field at a constant shear rate, the shear term always contributes, whereas the balance of the spring force and electrophoretic mobility terms varies with Wi_E. At low Wi_E, the migration does not significantly alter the spring distribution which is determined by the shear. However, at high Wi_E, the migration itself alters the spring distribution leading to a self-limiting migration. Schematically, this mechanism is described in Fig. 1. Finally, we compared our model to experimental data presented in Ref. [9] and found that our results were near quantitative at predicting the conditions for maximum migration.

It should be noted that this model is designed to study phenomena at relatively low shear rates and electric field strengths. At higher shear rates and electric fields, other phenomena will also couple with the mechanism described here. For example, hydrodynamic migration becomes significant at higher shear rates [4]. Furthermore, at high electric field strengths, charged polymers can collapse [22], impacting its electrophoretic mobility.

ACKNOWLEDGMENT

We gratefully acknowledge support from NSF Grant No. CBET 1826788.

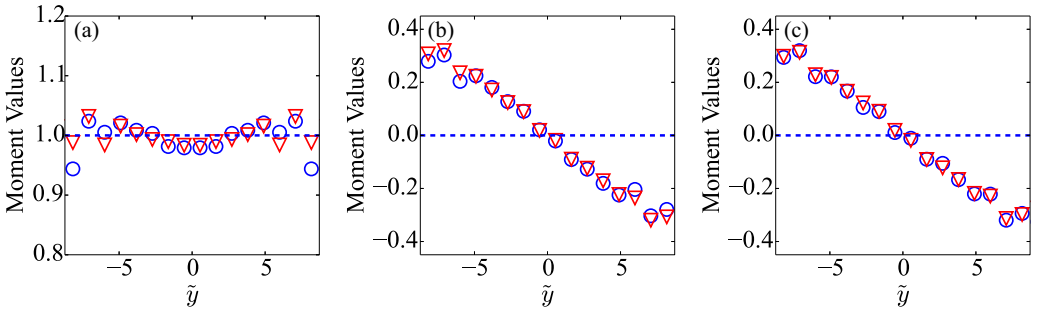

FIG. 5. Validation of the three closures for $\mathrm{Wi}_E = 25$ and $\mathrm{Wi}_F = 0.6$. The red triangles show the fourth order moments given by (a) $\langle \tilde{Q}_y^2 \tilde{Q}_y^2 \rangle$, (b) $\langle \tilde{Q}_x \tilde{Q}_y^3 \rangle$, and (c) $\langle \tilde{Q}_x^3 \tilde{Q}_y \rangle$. The blue circles give the corresponding approximations using second order moments from Eqs. (A4)–(A6). All data are from BD simulations. The horizontal blue dashed lines show the equilibrium value (the no flow no field case).

APPENDIX A: CLOSURE

In order to solve Eqs. (22)–(24), it is necessary to develop some expression for the fourth order moments. We found that assuming that the fourth order moments kept their equilibrium values and that the diffusive flux could be neglected gave excellent agreement with our simulations. To demonstrate the validity of this approximation, we take a different approach here. Equations (22)–(24) are first simplified via the order of magnitude analysis from the BD simulations described in Appendix B. The resultant equations are

$$24\tilde{n}\left[\langle \tilde{Q}_y^2 \rangle \tilde{\gamma} - \langle \tilde{Q}_x \tilde{Q}_y \rangle\right] = \frac{d}{d\tilde{y}}\left(\tilde{n}\Phi \langle \tilde{Q}_x^2 \tilde{Q}_y^2 \rangle\right), \tag{A1}$$

$$\left[1 - \langle \tilde{Q}_y^2 \rangle\right] = 0, \tag{A2}$$

$$2\tilde{\gamma}\langle \tilde{Q}_x \tilde{Q}_y \rangle + \left[1 - \langle \tilde{Q}_x^2 \rangle\right] = 0. \tag{A3}$$

These equations were solved in Sec. IV B by assuming the fourth order moment in Eq. (A1) remains at equilibrium. Instead, we here use a closure in order to capture out of equilibrium behavior. Moment closures have also been used to understand migration processes in swimming active matter systems [23–25], although the mechanism for migration is different. The approximation used here incorporates the correlation between the connector vector components in the x and y directions in weak shear flows and the combinatorial factors when grouping terms and takes the form

$$\langle \tilde{Q}_y^2 \tilde{Q}_x^2 \rangle \approx \langle \tilde{Q}_y^2 \rangle \langle \tilde{Q}_x^2 \rangle + 2\langle \tilde{Q}_x \tilde{Q}_y \rangle^2, \tag{A4}$$

$$\langle \tilde{Q}_y^3 \tilde{Q}_x \rangle \approx 3\langle \tilde{Q}_x \tilde{Q}_y \rangle \langle \tilde{Q}_y^2 \rangle, \tag{A5}$$

$$\langle \tilde{Q}_y \tilde{Q}_x^3 \rangle \approx 3\langle \tilde{Q}_x \tilde{Q}_y \rangle \langle \tilde{Q}_x^2 \rangle. \tag{A6}$$

The latter two approximations are not needed to solve Eqs. (A1)–(A3) but are included for completeness.

In order to gauge the accuracy of these approximations, we calculated both the second and the fourth order moments from our BD simulations and compared them in accordance with Eqs. (A4)–(A6). The results are shown in Fig. 5. As can be seen, there is excellent agreement between the fourth order moments and the corresponding combinations of second order moments. Although the channel coordinate goes from -21.775 to 21.775, we have only included the central portion of the channel where there was sufficient statistics to predict accurate data due to the migration. Furthermore, we have plotted the equilibrium value for the fourth order moments and see that the BD simulations show only mild deviations away from those values under these conditions.

Having validated the closure, Eq. (A4) can then be plugged into Eq. (A1) to produce a set of coupled equations. Using Eqs. (A2) and (A3) to eliminate $\langle \tilde{Q}_y^2 \rangle$ and $\langle \tilde{Q}_x^2 \rangle$, and using Eq. (20) results in

$$\frac{24}{\Phi}(\tilde{\gamma} - \langle \tilde{Q}_x \tilde{Q}_y \rangle) = \Phi \langle \tilde{Q}_x \tilde{Q}_y \rangle (1 + 2\tilde{\gamma}\langle \tilde{Q}_x \tilde{Q}_y \rangle + 2\langle \tilde{Q}_x \tilde{Q}_y \rangle^2) + \frac{d}{d\tilde{y}}(1 + 2\tilde{\gamma}\langle \tilde{Q}_x \tilde{Q}_y \rangle + 2\langle \tilde{Q}_x \tilde{Q}_y \rangle^2). \tag{A7}$$

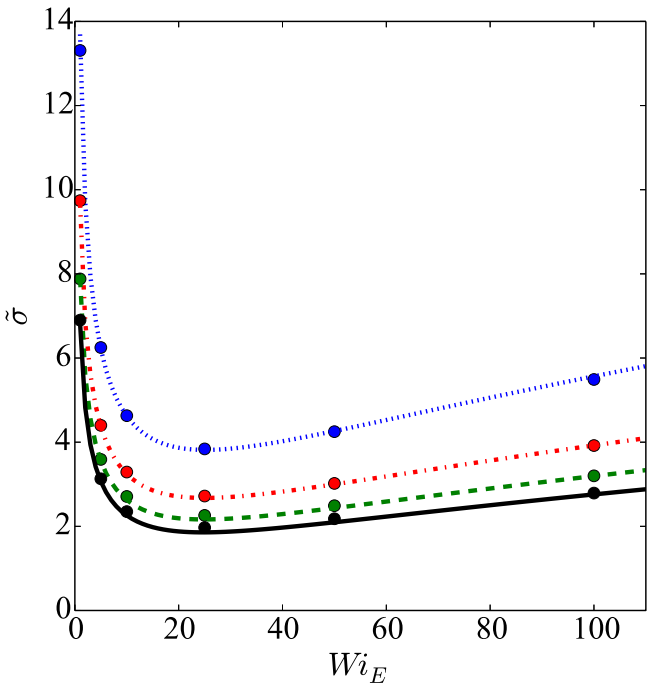

FIG. 6. The standard deviation of polymer concentration distributions as a function of Wi_F and Wi_E. The circles show the data from our BD simulations and are the same as in Fig. 3. The solid curves are predictions for $\tilde{\sigma}$ making use of Eqs. (A11) and (A12). The small difference between these curves and those in Fig. 3 is from relaxing the assumption about a fourth moment and using a closure approximation. The values of Wi_F are $\mathrm{Wi}_F = 0.3$ (blue dashed line), $\mathrm{Wi}_F = 0.6$ (red dot-dashed line), $\mathrm{Wi}_F = 0.9$ (green dashed line), and $\mathrm{Wi}_F = 1.2$ (black line).

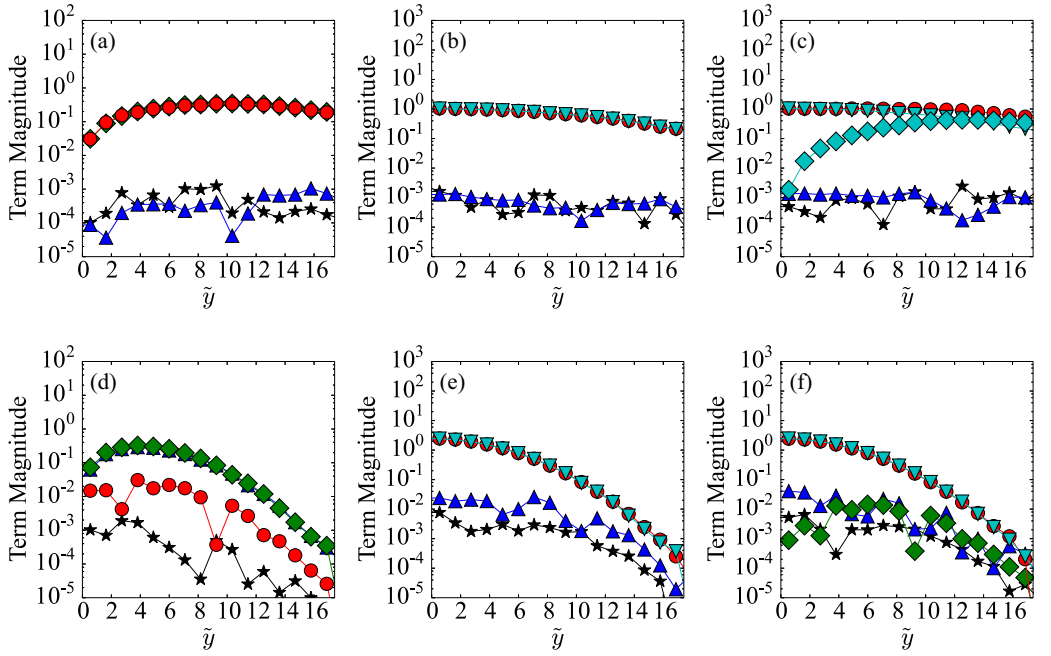

FIG. 7. The calculated values from the BD simulations for each term in Eqs. (22)–(24). The top row corresponds to $\mathrm{Wi}_F = 0.6$ and $\mathrm{Wi}_E = 1$. (a) shows the components of Eq. (22), (b) shows the components of Eq. (23), and (c) shows the components of Eq. (24) under these conditions. The bottom row corresponds to $\mathrm{Wi}_F = 0.6$, $\mathrm{Wi}_E = 100$. (d) shows the components of Eq. (22), (e) shows the components of Eq. (23), and (f) shows the components of Eq. (24) under these conditions. The terms displayed include migratory flux (blue upward facing triangles), diffusive flux terms (black stars), shear (green diamonds), spring extension (red circles), and Brownian diffusion (cyan downward facing triangles).

The variability of the shear rate with position can be shown explicitly by writing $\tilde{\gamma} = 2\,\mathrm{Wi}_F\tilde{y}/\tilde{H}$, which results in

$$\left[-\frac{48\,\mathrm{Wi}_F\tilde{y}}{\tilde{H}\Phi}\right] = \frac{24}{\Phi}\langle\tilde{Q}_x\tilde{Q}_y\rangle + \Phi\langle\tilde{Q}_x\tilde{Q}_y\rangle \times\left(1-\frac{4\,\mathrm{Wi}_F\tilde{y}}{\tilde{H}}\langle\tilde{Q}_x\tilde{Q}_y\rangle + 2\langle\tilde{Q}_x\tilde{Q}_y\rangle^2\right) + \frac{d}{d\tilde{y}}\left(1-\frac{4\,\mathrm{Wi}_F\tilde{y}}{\tilde{H}}\langle\tilde{Q}_x\tilde{Q}_y\rangle + 2\langle\tilde{Q}_x\tilde{Q}_y\rangle^2\right). \tag{A8}$$

The solution in the center of the channel can be computed using a Taylor series incorporating the odd symmetry using the form

$$\langle\tilde{Q}_x\tilde{Q}_y\rangle \approx -a_1\tilde{y} + a_3\tilde{y}^3 + \cdots, \tag{A9}$$

where a_1 and a_3 are undetermined coefficients. We found that only the first order term contributed significantly and all other terms could be dropped. By plugging Eq. (A9) into Eq. (A8) we can solve for a_1 and, by extension, $\langle\tilde{Q}_x\tilde{Q}_y\rangle$. The coefficient a_1 must satisfy

$$0 = 4a_1^2 - \left[\frac{24}{\Phi} + \Phi - \frac{8\,\mathrm{Wi}_F}{\tilde{H}}\right]a_1 + \frac{48\,\mathrm{Wi}_F}{\tilde{H}\Phi}, \tag{A10}$$

which can be solved yielding

$$a_1 = \frac{\left(\frac{24}{\Phi} + \Phi - \frac{8\,\mathrm{Wi}_F}{\tilde{H}}\right) - \sqrt{\left(\frac{24}{\Phi} + \Phi - \frac{8\,\mathrm{Wi}_F}{\tilde{H}}\right)^2 - \frac{768\,\mathrm{Wi}_F}{\Phi\tilde{H}}}}{8}. \tag{A11}$$

This solution can be plugged back into Eq. (A9) to get an expression for $\langle\tilde{Q}_x\tilde{Q}_y\rangle$. In turn, this can be used to calculate $\tilde{\sigma}$ for the distributions using Eq. (20) as in the body of the paper, which is given by

$$\tilde{\sigma} = \frac{1}{\sqrt{\Phi a_1}}. \tag{A12}$$

A comparison between this prediction and the BD simulations is shown in Fig. 6. For small Wi_F, Eqs. (A12) and (28) become the same and match with the BD simulations across all values of Wi_E. For larger Wi_F, Eq. (A12) more accurately captures the distortion of the fourth moments from equilibrium but matches the BD simulations comparably well, demonstrating the validity of our original assumption.

APPENDIX B: SIMPLIFICATION OF THE SYSTEM OF DIFFERENTIAL EQUATIONS

In this paper, we showed that our kinetic theory adequately captures the migration of the polymers and we could solve the kinetic theory more easily if we made assumptions about the importance of terms within the theory. In this Appendix, we use the BD simulations to validate assumptions made in the kinetic theory. In the BD simulations, the polymer concentration and moments are computed for each region of $\tilde{y}$, and derivatives are computed from them using central finite difference. The results are shown in Fig. 7. We show two conditions: one at low electric field strength [$\mathrm{Wi}_E = 1$, Figs. 7(a)–7(c)] and one at high electric field strength [$\mathrm{Wi}_E = 100$, Figs. 7(d)–7(f)]. This was performed in order to demonstrate how the magnitude of certain terms were significant

whereas other terms could not be neglected over a range of Wi_E.

Due to the many terms in Eqs. (22)–(24), it is useful to note that, on the right hand side of the equations, the terms containing the first derivative and fourth moments resulted from the electrophoretic migratory flux and terms containing the second derivatives represent diffusive flux. On the left hand side, we distribute the $24\tilde{n}$ term onto the terms within the brackets for these results. The terms containing $\tilde{\gamma}$ represent shear distorting the spring distribution, the second order moments represent the spring force acting to push the spring distribution towards equilibrium, and the terms with 1 represent Brownian diffusion.

In all cases, the diffusive terms (black stars) are small. This supports the assumption made in Sec. IV B and Appendix A that the diffusive terms could be neglected. Similarly, the migratory flux terms(blue upwards triangles) are small in Figs. 7(b), 7(c) 7(e), and 7(f), which validates our assumption that the fourth order moments for Eqs. (23) and (24) would be close to their equilibrium values of 0. However, the fourth order moment term in Eq. (22) contributes significantly in the high Wi_E case [Fig. 7(d)] but not for the low Wi_E case [Fig. 7(a)]. Because the fourth order moment does contribute significantly at higher Wi_E, this warrants its inclusion to the system of equations as in Sec. IV B.

Furthermore, Figs. 7(a) and 7(d) show that, although the shear is significant at both high and low Wi_E's, the magnitude of the other terms differs. At high Wi_E's, the shear contribution is matched by the fourth order moment term. At low Wi_E's, the shear contribution is balanced by the spring extension term. As Wi_E increases, so does the fourth order moment's term, whereas the spring extension term decreases. This trend continues until the behavior shown in Fig. 7(d) manifests.

These quantifications using the BD simulations of the terms in Eqs. (22)–(24) validate which phenomena are important and how they are rewritten as Eqs. (A1)–(A3) in Appendix A.

[1] J. Zheng and E. S. Yeung, Anal. Chem. **74**, 4536 (2002).
[2] J. Zheng and E. S. Yeung, Anal. Chem. **75**, 3675 (2003).
[3] L. Fang, H. Hu, and R. G. Larson, J. Rheol. **49**, 127 (2005).
[4] H. Ma and M. D. Graham, Phys. Fluids **17**, 083103 (2005).
[5] O. B. Usta, J. E. Butler, and A. J. Ladd, Phys. Fluids **18**, 031703 (2006).
[6] R. M. Jendrejack, D. C. Schwartz, J. J. De Pablo, and M. D. Graham, J. Chem. Phys. **120**, 2513 (2004).
[7] O. B. Usta, J. E. Butler, and A. J. C. Ladd, Phys. Rev. Lett. **98**, 098301 (2007).
[8] H. Pandey, S. A. Szafran, and P. T. Underhill, Soft Matter **12**, 3121 (2016).
[9] M. Arca, J. E. Butler, and A. J. Ladd, Soft Matter **11**, 4375 (2015).
[10] R. J. Montes, J. E. Butler, and A. J. Ladd, Electrophoresis **40**, 437 (2019).
[11] M. Arca, A. J. Ladd, and J. E. Butler, Soft Matter **12**, 6975 (2016).
[12] W.-C. Liao, N. Watari, S. Wang, X. Hu, R. G. Larson, and L. J. Lee, Electrophoresis **31**, 2813 (2010).
[13] H. Pandey and P. T. Underhill, Phys. Rev. E **92**, 052301 (2015).
[14] R. Kekre, J. E. Butler, and A. J. C. Ladd, Phys. Rev. E **82**, 050803(R) (2010).
[15] J. E. Butler, O. B. Usta, R. Kekre, and A. J. Ladd, Phys. Fluids **19**, 113101 (2007).
[16] P. Grassia, E. Hinch, and L. Nitsche, J. Fluid Mech. **282**, 373 (1995).
[17] D. L. Ermak and J. McCammon, J. Chem. Phys. **69**, 1352 (1978).
[18] P. S. Doyle and P. T. Underhill, *Handbook of Materials Modeling* (Springer, Berlin, 2005), pp. 2619–2630.
[19] H. R. Warner, Jr., Ind. Eng. Chem. Fundam. **11**, 379 (1972).
[20] R. B. Bird, R. C. Armstrong, and O. Hassager, *Dynamics of Polymeric Liquids, Vol. 2: Kinetic Theory* (Wiley, New York, 1987).
[21] E. S. Shaqfeh, J. Non-Newtonian Fluid Mech. **130**, 1 (2005).
[22] J. Tang, N. Du, and P. S. Doyle, Proc. Natl. Acad. Sci. USA **108**, 16153 (2011).
[23] D. Saintillan and M. J. Shelley, in *Complex Fluids in Biological Systems: Experiment, Theory, and Computation*, edited by S. E. Spagnolie (Springer, New York, 2015), pp. 319–355.
[24] B. Ezhilan and D. Saintillan, J. Fluid Mech. **777**, 482 (2015).
[25] W. Yan and J. F. Brady, J. Fluid Mech. **785**, R1 (2015).